Target Prior-enriched Implicit 3D CT Reconstruction with Adaptive Ray Sampling

Qinglei Cao[1†], Ziyao Tang[1†], and Xiaoqin Tang[1*]

[1] College of Computer and Information Science, Southwest University, Chongqing 400715, China
tangx0530@swu.edu.cn

Abstract. Existing implicit 3D reconstruction methods utilizing NeRF and its variants for internal CT often overlook anatomical priors of target objects, limiting accuracy in ultra-sparse view scenarios. We present TP-INR, a novel framework that leverages sparse-view projections to generate high-quality anatomical priors for structural encoding of objects. By combining prior-based structural encoding with positional encoding, TP-INR enhances implicit representations for precise CT reconstruction with minimal supervision in these challenging conditions. Additionally, we tailor the implicit framework for medical applications through refined network design and adaptive ray-based training, improving both accuracy and efficiency. Experimental results across various organ regions demonstrate that TP-INR outperforms state-of-the-art methods in reconstruction quality and efficiency, relying solely on projection data. Code is available upon request.

Keywords: CBCT · Sparse view · Implicit neural representation.

1 Introduction

In recent years, the rapid advancement of Cone-Beam Computed Tomography (CBCT) has intensified concerns regarding the radiation exposure associated with X-rays. Current research addresses these concerns by focusing on reducing radiation doses and the number of projections. This paper emphasizes the latter, aiming for high-quality CBCT reconstruction with ultra-sparse views. Traditional analytical methods, such as FBP [10] and various iterative algorithms [16], often produce suboptimal results for sparse-view CT reconstruction. Fully-supervised learning approaches encounter challenges related to data acquisition and generalizability [23,9,6,25,12,18,13,15]. In 2020, Ben et al. introduced Neural Radiance Fields (NeRF) [14], paving the way for innovative implicit 3D CT reconstruction. Since then, researchers have adapted NeRF for sparse-view CT reconstruction, creating new approaches grounded in X-ray imaging principles.

Despite progress, reconstruction methods for ultra-sparse scenarios still encounter several issues. (1) State-of-the-art methods like NAF [24] and SAX-NeRF

[1] †These authors contributed equally to this work. *Corresponding author.

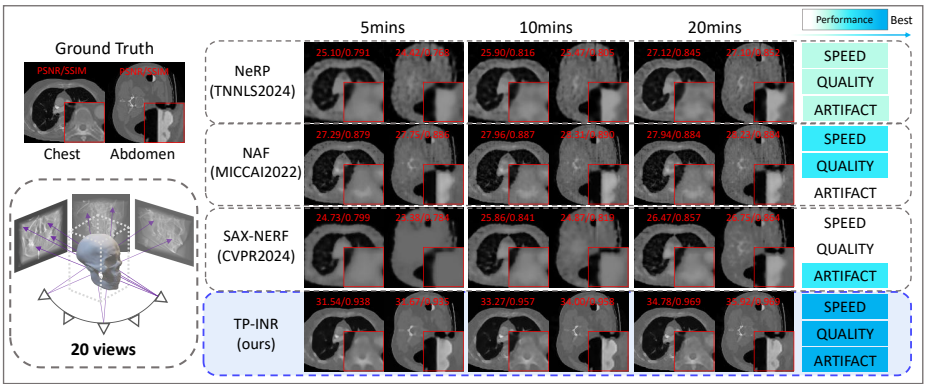

Fig. 1. Sparse-view 3D CT reconstruction with the state-of-the-art methods. Comparisons using NeRP [17], NAF [24], and SAX-NeRF [2] highlights our superior performance in learning efficiency, reconstruction precision, and artifact removal.

[2] improve learning efficiency through per-ray processing but sacrifice quality due to position encodings optimized for smaller networks. In contrast, NeRP [17] achieves better quality at the cost of increased time complexity and reliance on additional priors. (2) Networks that depend solely on positional encoding often produce low-resolution, overly smooth reconstructions, lacking detail and introducing artifacts due to inadequate supervision. (3) Recent methods utilized approximate priors to pre-train implicit neural representation (INR) networks. Typically, these priors are derived from similar body parts across different individuals or time points [17,3]. Although this technique improves reconstruction accuracy, its practical application in engineering contexts is still limited.

To tackle these challenges, we present an innovative implicit CT reconstruction method, TP-INR. (1) Our approach prioritizes reconstruction accuracy and learning efficiency through a specialized INR architecture tailored for medical imaging. Distinct from existing models, TP-INR integrates prior-based structural encoding and a refined network design to enhance accuracy using only project data, while an adaptive ray-based training strategy boosts efficiency, creating a solid framework for ill-posed CT reconstruction. (2) TP-INR enhances position encoding by incorporating target priors for structural encoding, providing additional structural insights for high-quality reconstruction with minimal supervision. (3) We define 'target prior' as anatomical priors derived from an object's projection data, allowing for object-specific prior assignment that eliminates the need for approximate priors, thereby enhancing practical usability. As shown in Fig. 1, IP-INR surpasses current state-of-the-art methods in both quality and efficiency across evaluated metrics. The key contributions are summarized as follows:

– We propose TP-INR, a specialized implicit model for ultra-sparse CBCT reconstruction using only projection data. By integrating prior-based struc-

tural and positional encoding for voxels on adaptively sampled rays, TP-INR enhances reconstruction accuracy and efficiency with minimal supervision.
– We developed a CUDA-based Target Prior Estimator (TPE) that rapidly derives high-quality target priors, enabling reliable anatomical prior assignment to sampled voxels and improving structural encoding.

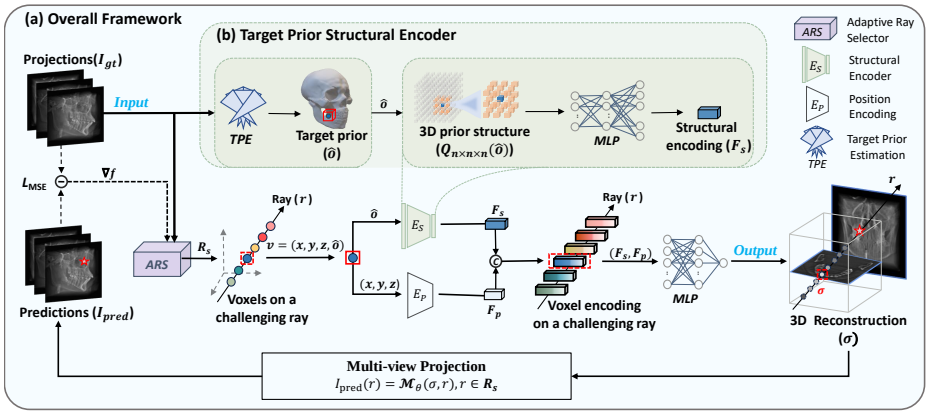

Fig. 2. Overview of the TP-INR 3D CT Reconstruction Network. (a) The model identifies challenging rays from input projections using the ARS strategy, guided by loss values. Each voxel along these rays is encoded with target prior structure and positional information (E_S and E_P), which are fused to create an implicit neural representation for CT image reconstruction and multi-view loss calculation in projection domain. (b) The TPSE module estimates target prior from projections via the TPE algorithm.

2 Methodology

2.1 Overall Framework

Fig. 2(a) illustrates the architecture of our TP-INR model, taking sparse-view projections (I_{gt}) as input and outputs a reconstructed 3D volume (σ). Inspired by Hard Sample Mining [19], we employ an Adaptive Ray Selector (ARS) to target challenging rays for efficient model training. The ARS strategy traces rays from the input projections, evaluates their projection domain losses (∇f), and identifies challenging rays (R_s) for targeted training, defined as $R_s = \text{ARS}(I_{\text{gt}}, \nabla f)$. Given a challenging ray $r \in R_s$, it defines each voxel along r as $v = (x, y, z, \hat{o})$, $v \in r$, where (x, y, z) is the spatial position and $\hat{o}$ denotes a target prior, which provides positional and structural encodings for implicit learning. The INR network then learns the mapping function between the encoded representation of v for individual voxels and their intensity distribution σ, expressed as:

$$\sigma = \text{Rec}(v; \boldsymbol{\phi}) = \text{Rec}(x, y, z, \hat{o}; \boldsymbol{\phi}), \quad v \in R_s. \tag{1}$$

It utilizes E_P for positional encoding and E_S for prior-based structural encoding. The positional encoding F_p is obtained by encoding the point $p = (x, y, z)$ using a Gaussian Fourier encoder γ, which is particularly effective in capturing intricate medical details [22]. Following this encoding, a two-layer multi-layer perceptron (MLP) network f_p with parameters ϕ_1 is employed to represent the positional features. Thus, $F_p = E_P(x, y, z) = f_p(\gamma(p); \phi_1)$. The prior-based structural encoding F_s is obtained from our Target Prior Structural Encoder (TPSE) module which comprises both prior estimation and structural encoding, as shown in Fig. 2(b), represented by $F_s = E_S(\hat{o})$. The details of the TPSE module will be elaborated in the section 2.2. The positional and structural feature encodings, F_p and F_s, are subsequently concatenated and fed into a MLP network (with parameters ϕ_3) for implicit learning. This network predicts the radiance density σ at each voxel along the ray with $\sigma = MLP\left(Concat(F_p, F_s); \phi_3\right)$, adopting Sine Activation function [20] in fully connected layers and Sigmoid activation in the final layer to ensure the non-negativity of the predicted reconstruction results.

According to the Beer-Lambert law [21], the intensity of an X-ray decreases as it passes through an object due to the exponential integral of the radiance density. We discretize it and apply it to our model, obtaining:

$$I_{\text{pred}}(r) = \mathcal{M}_\theta(\sigma, r) = I_0 \cdot \left(1 - e^{-\sum_{p=1}^{P} \sigma_p t_p}\right) \tag{2}$$

where σ_p denotes the predicted radiance density of voxel p, t_p represents the distance between two adjacent voxels, and P is the total number of voxels along the ray path r. We define $\mathcal{M}_\theta(\sigma, r)$ as the projection function of the ray r in the θ direction, which intersects an object with radiance densities of σ. The corresponding values in the prediction domain are denoted as $I_{\text{pred}}(r)$. With this multi-view projection function, we compute the $L2$ loss between the predicted projections of challenging rays ($r \in R_s$) and their ground truth for model training:

$$L_{\text{MSE}} = \frac{1}{|R_s|} \sum_{r \in R_s} \|I_{\text{pred}}(r) - I_{\text{gt}}(r)\|_2^2 \tag{3}$$

2.2 Target Prior Structural Encoder

As shown in Fig. 2(b), the structural feature encoding F_s encapsulates an object's target prior $\hat{o}$ produced by our TPE algorithm using the structure encoder E_S. At position $p = (x, y, z)$, we extract its anatomic structure ($Q_{n\times n\times n}(\hat{o}_p)$) for structural encoding, with $Q_{n\times n\times n}$ being its n-sized neighborhood. Subsequently, F_s is obtained through a two-layer MLP network (f_s) parameterized by ϕ_2, expressed as $F_s = E_S(\hat{o}) = f_s(Q_{n\times n\times n}(\hat{o}_p); \phi_2)$.

The quality of target prior ($\hat{o}$) estimated from projections significantly impacts the structural encoding F_s and the final radiance density σ. This necessitates high-quality estimates of $\hat{o}$ while also prioritizing time efficiency. To address this, we developed our TPE algorithm (see Algorithm 1), which iteratively estimates priors for voxels along challenging rays using CUDA. Starting with the projections I_{gt}, the algorithm performs multiple forward projections and

Algorithm 1 TPE: Target Prior Estimator

Input: I_{gt}, K, λ_1; $\mathcal{M}_\theta()$

Initialize $\hat{o} = \text{Count} = O \in R^3, \nabla f = O \in R$
for $j = 1, \ldots, K$ **do**
  Select challenging rays with ARS strategy:
  $R_s^j = \text{ARS}(I_{\text{gt}}, \nabla f)$
  Calculate the challenging rays' projection losses:
  $I_{\text{pred}}(R_s^j) = \mathcal{M}_\theta(\hat{o}^j, R_s^j)$
  $\nabla f = I_{\text{gt}}(R_s^j) - I_{\text{pred}}(R_s^j)$
  Determine voxels' update rate and Local Variation:
  $\text{step}_p = \frac{\max(\text{Count}^j)}{\text{Count}_p^j}, p = (x, y, z) \in R_s^j$
  $LV(\hat{o}_p^j) = \text{aver}(Q_{m\times m\times m}(\hat{o}_p^j)) - \hat{o}_p^j$
  Compute the update gradient for challenging voxels:
  $\mu = \nabla f \cdot \text{step}_p + \lambda_1 \cdot LV(\hat{o}_p^j), p \in R_s^j$
  Update the target prior for the challenging voxels:
  $\hat{\mathbf{o}}_p^{j+1} = \hat{\mathbf{o}}_p^j + \mu, p \in R_s^j$
  Update the sampling count for the challenging voxels:
  $\text{Count}_p^{j+1} = \text{Count}_p^j + 1, p \in R_s^j$
end for

Output: $\hat{\mathbf{o}} = \hat{\mathbf{o}}^K$

backward updates, progressively minimizing reconstruction errors and yielding a target prior for individual voxels. The iterative backward update process is defined as follows:

$$\hat{o}_p^{j+1} = \hat{o}_p^j + \mu, p \in R_s^j \tag{4}$$

where j is the iteration number, and μ updates $\hat{o}$ for voxel $p \in R_s^j$, expressed as:

$$\mu = \nabla f \cdot \text{step}_p + \lambda_1 \cdot LV(\hat{o}_p), p \in R_s^j. \tag{5}$$

Here, ∇f signifies the difference between the predicted projection and the ground truth, serving as the gradient for updating $\hat{o}$ along each challenging ray. To tackle uneven voxel sampling, which can affect convergence rates and lead to local optima, we introduce an adaptive update rate, step_p, defined as: $\text{step}_p = max(\text{Count}^j)/\text{Count}_p^j$. This formula adjusts the update rate for voxel p based on its sampling count relative to the maximum across all voxels, enhancing convergence consistency throughout the dataset. Additionally, discrete ray sampling points can make voxels along the ray path susceptible to outliers (high-frequency noise) during updates. To counteract this, we apply Local Variation (LV) [5] to correct μ: $LV(\hat{o}_p) = \text{aver}(Q_{m\times m\times m}(\hat{o}_p)) - \hat{o}_p$, where 'aver' denotes the averaging operation, and λ_1 is a constant weight.

The effectiveness of our TPE algorithm in rapidly (in seconds) achieving a high-quality target prior can be attributed to two main factors. First, each iteration refines the estimate based on the difference (∇f) between the predicted and measured projections, minimizing reconstruction error and ensuring convergence. Starting from a zero-like initializer enables more effective correction in

poorly reconstructed foreground voxels. Second, the LV serves as a regularization term to reduce noise from the projections, enhancing stability and accuracy. Our TPE algorithm generates the object's target prior $\hat{o}$, independently of the INR learning process. It occurs only once before the training or testing process, offering a task-relevant prior for structural encoding within TPSE.

3 Experiment

3.1 Experimental Settings

Dataset and Implementation Details: Experiments were conducted on the datasets that cover jaw, chest, abdomen, and foot regions. The chest data is from the LIDC-IDRI dataset [1], while the others are sourced from Open Scientific Visualization Datasets [11]. Our model, implemented in PyTorch with CUDA 10.1, runs on a RTX 3090 GPU. We utilize the Adam optimizer with a learning rate of 0.00001. In the TPE algorithm, parameters are set as: $\lambda_1 = 0.001, m = 3$ for the LV calculation, and each ray samples $P = 128$ voxels. To extract target prior structures, the neighbor size is $n = 5$, and the iteration count for fast prior estimation is $K = 50$. Ultra-sparse view projections were tested with 10, 20, and 30 views. Reconstruction quality was assessed using PSNR [7] and SSIM [8].

Table 1. Quantitative comparison of 3D cone-beam reconstructions across anatomies.

Data	Views	PSNR/SSIM					
		FDK	SART-TV	NeRP	NAF	SAX-NeRF	TP-INR
Jaw	10	20.40/.440	25.90/.725	28.17/.821	26.04/.750	26.59/.775	**30.10/.878**
	20	24.15/.616	28.61/.834	31.85/.912	29.59/.879	29.93/.888	**34.91/.955**
	30	26.75/.726	30.94/.895	34.48/.951	31.38/.920	32.42/.934	**37.69/.975**
Chest	10	15.56/.360	22.48/.727	26.83/.824	24.50/.787	24.44/.784	**29.54/.914**
	20	20.99/.550	25.56/.836	30.66/.913	27.93/.882	27.32/.873	**36.43/.978**
	30	24.24/.663	27.59/.889	31.75/.935	30.01/.925	29.80/.919	**39.59/.989**
Abdomen	10	16.72/.393	25.80/.794	25.20/.791	24.98/.803	24.80/.826	**29.49/.913**
	20	21.06/.535	28.56/.865	30.74/.918	28.20/.882	28.40/.899	**37.27/.976**
	30	23.92/.636	30.48/.908	32.95/.947	29.81/.911	30.01/.921	**40.49/.986**
Foot	10	17.92/.358	26.20/.854	26.97/.778	25.37/.856	27.20/.890	**30.81/.933**
	20	22.04/.439	29.31/.911	30.90/.889	29.15/.920	30.06/.932	**35.50/.972**
	30	24.92/.527	31.89/.946	33.03/.936	32.88/.957	32.62/.958	**38.05/.983**

3.2 Comparison Results

Quantitative Comparison: Table 1 provides a quantitative evaluation of the reconstruction results across various sparse-view projections. Given the challenges of obtaining approximate priors in practical applications—where only projection images are accessible—all methods compared rely solely on these projections for reconstruction. Taking the chest dataset as an example, TP-INR consistently outperforms traditional FDK [4], iterative SART-TV [23], and

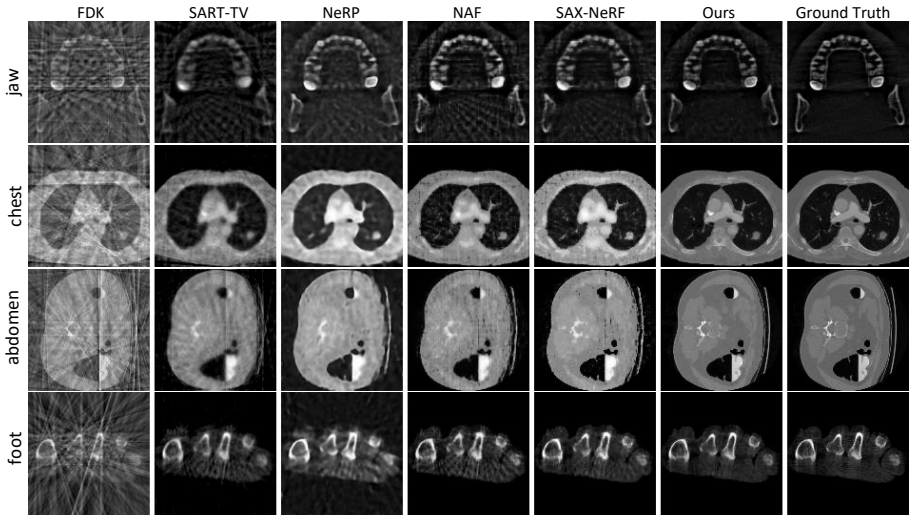

Fig. 3. Visual comparison of reconstructed images generated by various methods relying solely on 20 projection data across four distinct anatomical regions.

implicit methods such as NeRP [17], NAF [24], and SAX-NeRF [2], achieving the highest PSNR and SSIM across various sparse-view scenarios. For instance, with 20 projection views, TP-INR surpasses NeRP, NAF, and SAX-NeRF by 5.77 dB, 8.5 dB, and 9.11 dB in PSNR, respectively.

Visual Comparison: In Fig. 3, we present the visual performance of different methods for sparse-view CBCT reconstruction. Among implicit models, the performance of NeRP is adversely affected by artifacts and blurriness in the absence of approximate priors. Although NAF and SAX-NeRF have mitigated some of the artifacts present in NeRP, the overall image quality remains inadequate, with persistent noise and lost details. The proposed TPAR-INR surpasses the performance of these state-of-the-art techniques by preserving more details and effectively suppressing artifacts, resulting in more accurate reconstructions.

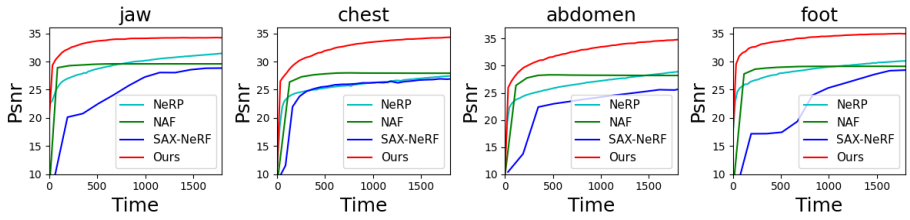

Fig. 4. Comparative analysis of learning efficiency by PSNR-Time (s) across methods

Learning Efficiency: In practical CT imaging systems, reconstruction time is a critical performance metric. Fig. 4 presents comparisons of Time-PSNR for NeRP, NAF, SAX-NeRF, and our method, all reconstructed using 20 projections across four 3D anatomical regions. Our method demonstrates the shortest reconstruction time while achieving a higher PSNR value. This efficiency can be largely attributed to our ARS strategy, which prioritizes the most challenging rays, facilitating effective learning, especially during the early stages of training.

3.3 Ablation Study on the ARS and TPSE module

Table 2 presents a comprehensive incremental ablation study on chest data, highlighting the contributions of our ARS and TPSE modules. This study demonstrates how these modules enhance reconstruction quality across various sparse-view strategies. We also evaluated the TPE algorithm against analytical and iterative methods—FDK, SART-TV, and TPE without the LV component—using our INR model without target priors as a baseline. As shown in Table 3, TPE with LV yields higher PSNR and SSIM values for target priors ($\hat{o}$), resulting in more accurate image reconstructions (σ). This enhancement stems from TPE's adaptive gradient updating, driven by ∇f and step_p, which minimizes reconstruction error and ensures convergence, along with LV's noise suppression. Notably, our baseline model also delivers reasonable performance due to its refined design and adaptive ray-based training strategy.

Table 2. Incremental Ablations: the evaluation of the ARS and TPSE modules.

baseline	ARS	TPSE	10	20	30
√			27.13/0.877	33.98/0.968	37.48/0.984
√	√		28.78/0.892	35.16/0.972	38.47/0.986
√		√	28.73/0.897	35.61/0.974	39.16/0.987
√	√	√	**29.54/0.914**	**36.43/0.978**	**39.41/0.988**

Table 3. Ablation study on TPE's effectiveness in generating target priors and enhancing reconstruction accuracy compared to traditional methods.

Views	Prior/Pred	baseline	FDK	SART-TV	TPE w/o LV	TPE
10	$\hat{o}$	–	15.56/0.360	22.48/0.727	22.83/0.689	**24.33/0.758**
	σ	27.13/0.877	27.83/0.874	28.32/0.885	28.55/0.889	**29.54/0.914**
20	$\hat{o}$	–	20.99/0.550	25.56/0.836	26.22/0.818	**29.12/0.907**
	σ	33.98/0.968	35.26/0.973	35.36/0.973	35.35/0.973	**36.43/0.978**
30	$\hat{o}$	–	24.24/0.663	27.59/0.889	29.01/0.889	**31.69/0.946**
	σ	37.48/0.984	38.82/0.987	38.20/0.985	38.22/0.986	**39.41/0.988**

4 Conclusions

This paper introduces TP-INR, an INR model designed for ultra-sparse view CBCT reconstruction. TP-INR enhances both reconstruction accuracy and efficiency through a specialized architecture that integrates prior-based structural encoding, optimized network design, and adaptive ray-based training. By rapidly generating target priors from projection data, it achieves voxel structural encoding without the need for additional priors or pre-training, effectively addressing the information deficit in practical ultra-sparse imaging. Extensive empirical studies demonstrate that TP-INR surpasses existing methods in both quantitative and qualitative evaluations, establishing it as a leading solution for sparse-view CBCT reconstruction across various datasets and view configurations.

Acknowledgments. This work is supported by the National Natural Science Foundation of China Youth Found under Grant 62202391.

Disclosure of Interests. The authors have no competing interests to declare that are relevant to the content of this article.

References

1. Armato III, S.G., McLennan, G., Bidaut, L., McNitt-Gray, M.F., Meyer, C.R., Reeves, A.P., Zhao, B., Aberle, D.R., Henschke, C.I., Hoffman, E.A., et al.: The lung image database consortium (lidc) and image database resource initiative (idri): a completed reference database of lung nodules on ct scans. Medical physics **38**(2), 915–931 (2011)
2. Cai, Y., Wang, J., Yuille, A., Zhou, Z., Wang, A.: Structure-aware sparse-view x-ray 3d reconstruction. In: Proceedings of the IEEE/CVF Conference on Computer Vision and Pattern Recognition. pp. 11174–11183 (2024)
3. Du, C., Lin, X., Wu, Q., Tian, X., Su, Y., Luo, Z., Zheng, R., Chen, Y., Wei, H., Zhou, S.K., Yu, J., Zhang, Y.: Dper: Diffusion prior driven neural representation for limited angle and sparse view ct reconstruction (2024), `https://arxiv.org/abs/2404.17890`
4. Feldkamp, L.A., Davis, L.C., Kress, J.W.: Practical cone-beam algorithm. Josa a **1**(6), 612–619 (1984)
5. Felzenszwalb, P.F., Huttenlocher, D.P.: Image segmentation using local variation. In: Proceedings. 1998 IEEE Computer Society Conference on Computer Vision and Pattern Recognition (Cat. No. 98CB36231). pp. 98–104. IEEE (1998)
6. Han, Y., Ye, J.C.: Framing u-net via deep convolutional framelets: Application to sparse-view ct. IEEE transactions on medical imaging **37**(6), 1418–1429 (2018)
7. Hore, A., Ziou, D.: Image quality metrics: Psnr vs. ssim. In: 2010 20th international conference on pattern recognition. pp. 2366–2369. IEEE (2010)
8. Hwang, S.W., Sugiyama, J.: Computer vision-based wood identification and its expansion and contribution potentials in wood science: A review. Plant Methods **17**(1), 47 (2021)
9. Jin, K.H., McCann, M.T., Froustey, E., Unser, M.: Deep convolutional neural network for inverse problems in imaging. IEEE transactions on image processing **26**(9), 4509–4522 (2017)

10. Kak, A.C., Slaney, M.: Principles of computerized tomographic imaging. SIAM (2001)
11. Klacansky, P.: Open scientific visualization datasets (2022) (2022), http://klacansky.com/open-scivis-datasets/
12. Lee, H., Lee, J., Kim, H., Cho, B., Cho, S.: Deep-neural-network-based sinogram synthesis for sparse-view ct image reconstruction. IEEE Transactions on Radiation and Plasma Medical Sciences **3**(2), 109–119 (2018)
13. Li, Y., Li, K., Zhang, C., Montoya, J., Chen, G.H.: Learning to reconstruct computed tomography images directly from sinogram data under a variety of data acquisition conditions. IEEE transactions on medical imaging **38**(10), 2469–2481 (2019)
14. Mildenhall, B., Srinivasan, P.P., Tancik, M., Barron, J.T., Ramamoorthi, R., Ng, R.: Nerf: Representing scenes as neural radiance fields for view synthesis. Communications of the ACM **65**(1), 99–106 (2021)
15. Ronneberger, O., Fischer, P., Brox, T.: U-net: Convolutional networks for biomedical image segmentation. In: Medical image computing and computer-assisted intervention–MICCAI 2015: 18th international conference, Munich, Germany, October 5-9, 2015, proceedings, part III 18. pp. 234–241. Springer (2015)
16. Rudin, L.I., Osher, S., Fatemi, E.: Nonlinear total variation based noise removal algorithms. Physica D: nonlinear phenomena **60**(1-4), 259–268 (1992)
17. Shen, L., Pauly, J., Xing, L.: Nerp: Implicit neural representation learning with prior embedding for sparsely sampled image reconstruction. IEEE Transactions on Neural Networks and Learning Systems **35**(1), 770–782 (2024). https://doi.org/10.1109/TNNLS.2022.3177134
18. Shen, T., Li, X., Zhong, Z., Wu, J., Lin, Z.: Rˆ 2 2-net: Recurrent and recursive network for sparse-view ct artifacts removal. In: Medical Image Computing and Computer Assisted Intervention–MICCAI 2019: 22nd International Conference, Shenzhen, China, October 13–17, 2019, Proceedings, Part VI 22. pp. 319–327. Springer (2019)
19. Sheng, H., Zheng, Y., Ke, W., Yu, D., Cheng, X., Lyu, W., Xiong, Z.: Mining hard samples globally and efficiently for person reidentification. IEEE Internet of Things Journal **7**(10), 9611–9622 (2020)
20. Sitzmann, V., Martel, J., Bergman, A., Lindell, D., Wetzstein, G.: Implicit neural representations with periodic activation functions. Advances in neural information processing systems **33**, 7462–7473 (2020)
21. Swinehart, D.F.: The beer-lambert law. Journal of chemical education **39**(7), 333 (1962)
22. Tancik, M., Srinivasan, P., Mildenhall, B., Fridovich-Keil, S., Raghavan, N., Singhal, U., Ramamoorthi, R., Barron, J., Ng, R.: Fourier features let networks learn high frequency functions in low dimensional domains. Advances in neural information processing systems **33**, 7537–7547 (2020)
23. Wang, G., Ye, J.C., De Man, B.: Deep learning for tomographic image reconstruction. Nature machine intelligence **2**(12), 737–748 (2020)
24. Zha, R., Zhang, Y., Li, H.: Naf: neural attenuation fields for sparse-view cbct reconstruction. In: International Conference on Medical Image Computing and Computer-Assisted Intervention. pp. 442–452. Springer (2022)
25. Zhang, Z., Liang, X., Dong, X., Xie, Y., Cao, G.: A sparse-view ct reconstruction method based on combination of densenet and deconvolution. IEEE transactions on medical imaging **37**(6), 1407–1417 (2018)